# FireDrone: Multi-Environment Thermally Agnostic Aerial Robot

*David Häusermann,\* Sam Bodry, Fabian Wiesemüller, Aslan Miriyev, Severin Siegrist, Fan Fu, Sabyasachi Gaan, Matthias M. Koebel, Wim J. Malfait, Shanyu Zhao, and Mirko Kovač\**

Deploying robots in extreme environments reduces risks to human lives. However, robot operating conditions are often limited by environmental factors such as extreme temperatures encountered in fire disasters or polar regions. Especially drones face challenges in carrying thermal management systems protecting vital components, due to limited payload capacity compared to ground robots. Herein, a thermally agnostic aerial robot comprising structural thermally insulating material and a phase change material cooling system, inspired by natural thermal regulation principles, is designed, modelled and experimentally validated. Building on the robot development paradigm of physical artificial intelligence, the concurrent development of materials and design enables the creation of novel physiologically adaptive systems. Polyimide aerogel is applied as one of the main structural materials in the drone's design to adapt the robot's structure and properties to extreme temperatures. Glass fiber reinforcement with silica aerogel particles reduces high-temperature shrinkage and pore structure degradation after exposure to high temperatures and most of the composite aerogel features are preserved. A high technology-readiness-level drone prototype, allowing for operation in a broad range of ambient temperatures, is demonstrated. The proposed technology for thermally agnostic drones may unleash the great potential of aerial robotics in multiple industrial and research applications.

## 1. Introduction

Extreme temperatures pose great challenges to all living organisms and man-made objects. To survive in such hostile environments, natural organisms evolve and employ various principles of thermal regulation and physiological adaptions. For example, penguins absorb solar radiation through their black overcoat feathers while being insulated by down and fat layers to survive in polar conditions (**Figure 1**a).[1] A phenomenon utilized by spittle bugs is to insulate themselves from high temperatures by creating a foam layer, which not only insulates but also evaporates and cools down the microenvironment below the foam through the energy required for the phase change (Figure 1b).[2] Additional to their excellent insulation by fur, animals such as the Arctic fox have evolutionarily reduced their exposure to extreme temperatures through small physiological features (Figure 1c).[3]

On the contrary, man-made objects usually have a limited spectrum of capabilities initially fitted to a narrow range of environmental and operating conditions. The leading design approach in robotics has been developing a system that can perform a specific

D. Häusermann, F. Wiesemüller, A. Miriyev, M. Kovač
Laboratory of Sustainability Robotics
Empa - Swiss Federal Laboratories for Materials Science and Technology
8600 Dübendorf, Switzerland
E-mail: david.haeusermann@empa.ch; mirko.kovac@empa.ch

D. Häusermann, F. Wiesemüller, A. Miriyev, M. Kovač
Aerial Robotics Laboratory
Imperial College London
South Kensington Campus, London SW7 2AZ, UK

The ORCID identification number(s) for the author(s) of this article can be found under https://doi.org/10.1002/aisy.202300101.

S. Bodry, M. M. Koebel, W. J. Malfait, S. Zhao
Building Energy Materials and Components
Empa - Swiss Federal Laboratories for Materials Science and Technology
8600 Dübendorf, Switzerland

S. Siegrist, F. Fu
Laboratory for Thin Films and Photovoltaics
Empa - Swiss Federal Laboratories for Materials Science and Technology
8600 Dübendorf, Switzerland

S. Gaan
Laboratory for Advanced Fibers
Empa - Swiss Federal Laboratories for Materials Science and Technology
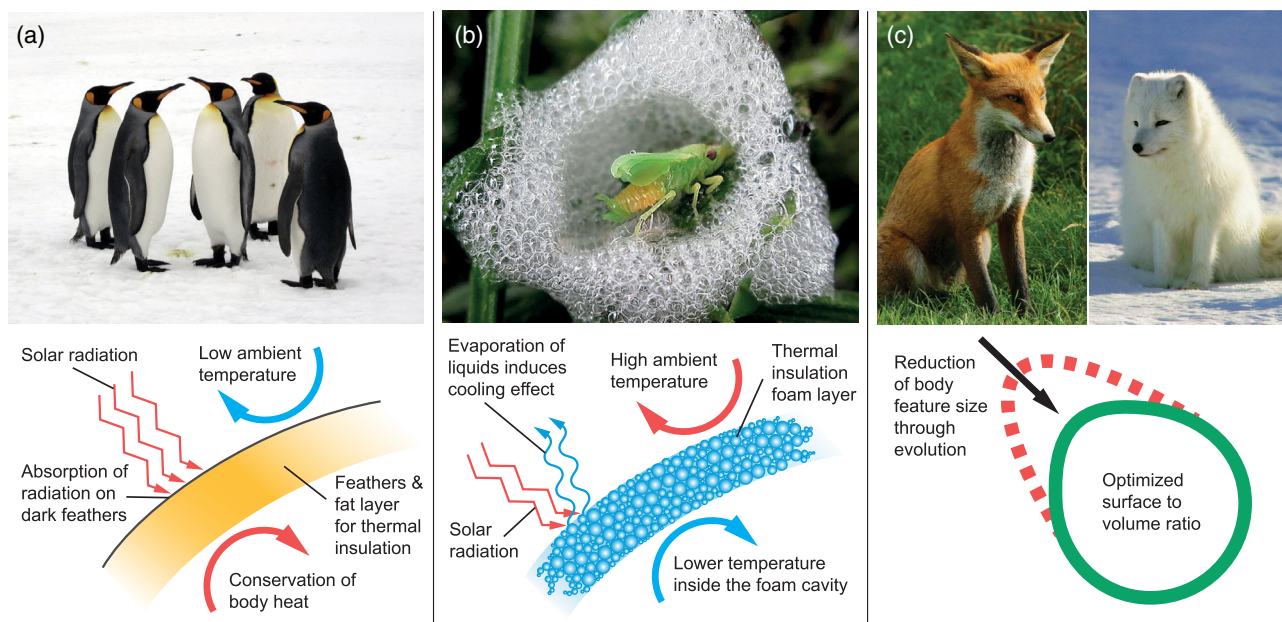9014 St. Gallen, Switzerland

**Figure 1.** Principles of thermal regulation for animals living in extreme temperature environments. a) Penguins: absorption of radiation on dark feathers and thermal insulation through down and fat layers (adapted from ref. [37]). b) Spittle bugs: thermal insulation through foam layer and evaporative cooling of the inside of the foam (adopted from ref. [38]). c) An arctic fox (right) compared to a red fox (left): thermal insulation through thick fur and smaller body features (ears, legs, snout) to minimize the surface area exposed to the arctic environment (adopted from refs. [39,40]).

set of preprogrammed tasks in specific environmental conditions. For instance, aerial robots of all sizes typically fly controllable in nonturbulent, mainly obstacle-free environments at a limited range of temperatures. The materials and systems comprising state-of-the-art aerial robots may face challenges while operating in extreme cold and hot environments since the limited payload capacity restricts the deployment of thermal regulation systems compared to ground-based robots. This especially prevents the broad application of aerial robots in firefighting, inspection of hot and cold industrial sites and polar activities. Numerous attempts have recently been made to protect aerial robots from the effect of unusual temperatures. A recent Chinese patent describes a drone with heating and insulation solutions allowing for the proper functionality of its systems, such as the battery, in cold conditions.[4] Alternatively, Myeong et al. report on covering the existing drone elements (frame, electronics unit, and motors) with a custom-designed and stitched aramid fiber fabric[5] to shield it from fire. The authors also intentionally left air "pockets" to serve as additional insulating buffers. This technology was patented in South Korea in 2016.[6] To create a new class of intelligent robotic systems capable of adapting to the environment, we propose a solution on the "physiological" level inspired by nature. For synthetic agents, such as aerial robots, this means developing the physical artificial intelligence (PAI) of their system[7] by combining the aspects of materials, design, and manufacturing to obtain a broad range of functional and structural properties. Building on the inspire–abstract–implement paradigms of bioinspiration,[8] Figure 1 highlights effective extreme temperature–coping mechanisms in nature that can be adapted and implemented in robotic systems operating in extreme environments.

Here, we design, model, and experimentally validate a thermally agnostic drone comprising a structural shell of thermally super-insulating material. Specifically, we demonstrate an aerial robot with exoskeletal components manufactured from polyimide (PI) aerogel composites with an ultralow thermal conductivity $<0.020\,\mathrm{W\,m^{-1}\,K^{-1}}$ compared to $<0.033\,\mathrm{W\,m^{-1}\,K^{-1}}$ for conventional insulation materials. Aerogel materials are an ideal thermal insulator when space and weight are limited and possess an exceptionally high strength-to-weight ratio,[9] finding mass application in various industries.[10,11] The proposed technology for thermally insulated drones may unleash the great potential of aerial robotics in multiple industrial and research applications with extreme environments. When considering extreme temperature drone applications, for example, for firefighting robotics, PI aerogel is a prime candidate. PIs are high-performance engineering polymers with inherent high decomposition temperatures ($\geq 550\,^{\circ}\mathrm{C}$), chemical resistance, low refractive indices, and low permittivity, with applications in robotic systems.[12,13] PIs are most often prepared by step–growth condensation polymerization of diamines and dianhydrides, and the resulting polyamic acid (PAA) is imidized thermally or chemically. To prepare an aerogel material, the solid content is controlled by adjusting the polymer concentration in an organic solvent, and the porous structure can be maintained by supercritical $CO_2$ drying[14,15] or ambient pressure drying.[16] State-of-the-art PI and PI–silica composite aerogels show excellent overall performance (thermal conductivity 0.014–0.018 $\mathrm{W\,m^{-1}\,K^{-1}}$, compression 3–50 MPa, and tensile 4–10 MPa) and widely adjustable physical and chemical properties.[14,15,17–19] This makes PI aerogels an ideal candidate for the fabrication of components that combine excellent thermal

**ADVANCED
SCIENCE NEWS**

www.advancedsciencenews.com

**ADVANCED
INTELLIGENT
SYSTEMS**
Open Access

www.advintellsyst.com

and mechanical properties required for aerial robots, where lightweight construction is essential.

## 2. Results and Discussion

The results section first highlights the design approach for the thermally agnostic drone. Subsequently, the PI aerogel synthesis and characterization as well as the drone system performance are shown in detail.

### 2.1. Thermally Agnostic Drone Design

The operation constraints for robots in extreme temperature environments are challenging. All components must either be rigorously shielded by thermal insulation, actively cooled, or able to sustain the environmental temperatures. While metallic components can sustain high temperatures, their weight greatly impacts the flight performance of aerial robots. Furthermore, heat-sensitive components such as batteries, electronics, and motors must be protected from the extreme temperature environment due to the limited operation temperature for commercial components.[20]

Therefore, the proposed robot concept features a quadrotor with a central glass-fiber reinforced polyimide (GFRPI) aerogel protective shell where all thermally sensitive components are consolidated. **Figure 2**a shows the electronics compartment located at the top, the drivetrain in the center and the batteries mounted in the bottom section of the shell, with the camera system facing the front in forward flight.

The drone is equipped with an red–green–blue (RGB) camera (Nano 2, RunCam Technology Co. Ltd., China) for footage in the visible range and an infrared (IR) camera (Lepton 3.5 core, Teledyne FLIR LLC, USA) for the detection of heat sources and visual feedback to the operator in case of fires with heavy smoke. A data-acquisition system (DACS) monitors the temperatures of critical components, such as the batteries and motors, inside the protective shell as well as the external temperature. The DACS comprises an Arduino Nano connected to three thermocouple amplifiers (MAX31855, Adafruit Industries, USA) in combination with thermocouples (K-type glass braid insulated, Adafruit Industries, USA). The DACS records the temperature with a rate of 1 Hz and actuates the internal cooling system to keep all components within their operating temperature margins. The cooling system exploits the latent heat of evaporation of the liquid $CO_2$ present in commercial $CO_2$ cartridges, inspired by the principle in nature to utilize the energy required for the phase change to cool down the environment (Figure 1b). Upon valve actuation, a system of small tubes distributes the gas to cool the critical components (Figure 2b).

The thermal insulation of the drone is composed of PI aerogel tiles (15 mm thickness), bonded to interlocking mounting frames additively manufactured from polyamide 12 (PA12) to form the exoskeleton, and foam insulation for the arms (Figure 2c). The exoskeletal shell comes in the shape of a rhombicuboctahedron. This geometrical shape consists of 18 squares and 8 equilateral triangles with a side length of 75 mm which, at this prototyping stage, is beneficial for the manufacturing of the aerogel tiles compared to curved sections. As a trade-off between manufacturing complexity and surface-to-volume ratio (ratio of sphere: $\frac{3}{r}$; rhombicuboctahedron: $\frac{3.22}{r^*}$, with $r^*$ corresponding to the circumradius of the octagon) this shape best conforms to the principle of minimizing the surface area to cope with extreme temperatures (Figure 1c). To reflect IR radiation of heat sources, the shell is additionally coated with a thin aluminum film (Figure S1, Supporting Information), reversing the principle of radiation absorption by penguins' feathers (Figure 1a).

The motors are mounted inside the insulating shell to protect the copper windings and magnets from damage by extreme
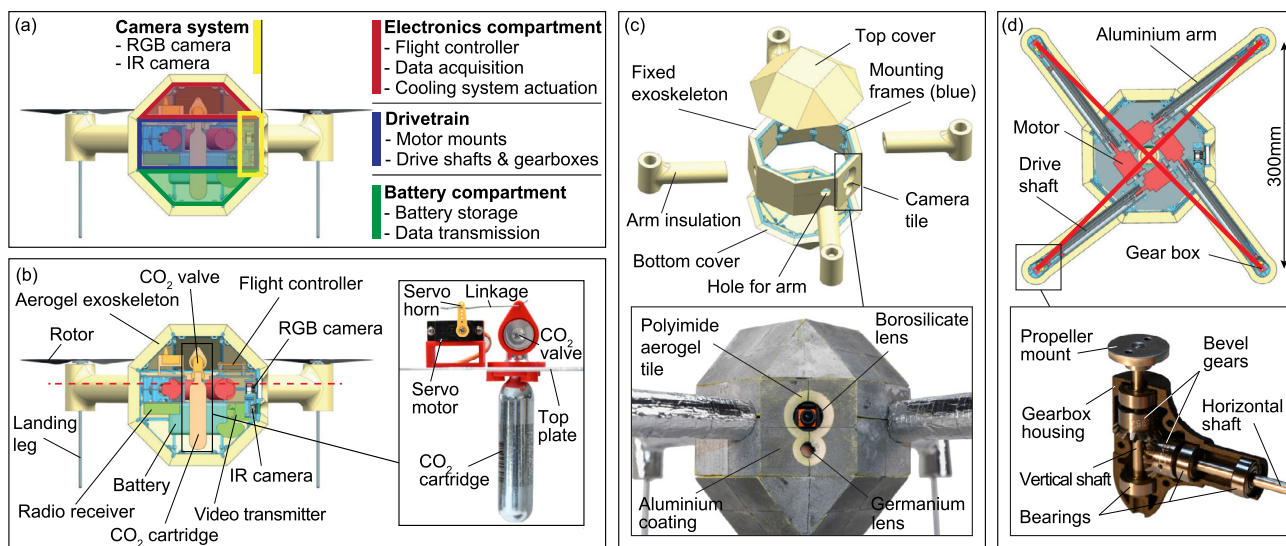


**Figure 2.** Overview of the drone design. a) System overview of compartments for electronics, drivetrain and batteries inside the aerogel composite exoskeleton. b) All temperature-sensitive components are protected inside the exoskeleton shell with a cooling system exploiting the thermodynamic behavior during the release and evaporation of gas from $CO_2$ cartridges. c) Exoskeleton shell tiles are manufactured from polyimide (PI) aerogel composites for low thermal conductivity with an aluminum coating for high reflection of thermal radiation. d) Drivetrain with a gearbox to protect and cool down the motors within the PI aerogel shell.

**ADVANCED
SCIENCE NEWS**

www.advancedsciencenews.com

**ADVANCED
INTELLIGENT
SYSTEMS**
Open Access

www.advintellsyst.com

temperatures. A mechanical drivetrain transmits the power through a gearbox (gear ratio of 1:1) to the rotors (Figure 2d).

The relationship between the air's temperature, density, and the factor of increased motor rotations per minute (rpm) to compensate for the reduced lift in the hot air is given in Figure S2, Supporting Information. Assuming an air temperature of 200 °C (maximum operating temperature of the aerogel insulation material without significant shrinkage and degradation, for detailed information, see Section 2.2), the air density is reduced by a factor of 1.6 to $\rho_{Air@200°C} = 0.745 \, kg \, m^{-3}$ compared to room temperature. The four brushless motors (FX2216-9 1100 kv, Lumenier Holdco LLC, USA) powered by two lithium polymer (LiPo) batteries wired in parallel (Tattu R-Line 2000 mAh 14.8 V, Grepow Inc., USA) transmit their power through a gearbox (45° bevel gear pair at a 1:1 ratio) to 9 inch propellers, resulting in a maximum allowable system weight of 2.4 kg to still maintain a stable hover position at the maximum allowable temperature of 200 °C. No mounting points for external payloads are implemented, since they would require additional insulation and the added mass would not only reduce the flight time but also the capability to fly at elevated ambient temperatures up to 200 °C.

To assess the heat flux from the high-temperature environment to the system, forced convection by the propeller downwash over the insulating shell is considered to then size the internal cooling system. Each of the four propellers generates a maximal lift force of $F_{hover} = 0.6 \, kg$ at 200 °C air temperature. With the momentum theory and the formula given in Equation (1), a first approximation of the resulting airspeed after the propeller can be obtained.[21]

$$v_{exit} = \sqrt{\frac{F}{0.5 \cdot \rho \cdot A} + v_{inlet}} \tag{1}$$

Herein, the exit velocity is given by $v_{exit}$, while $F$ corresponds to the generated force, $\rho$ to the air's density at 200 °C, $A$ to the area swept by the propeller, and $v_{inlet}$ to the air's velocity at the inlet. The resulting airspeed after the propeller during hovering of $v_{exit} \approx 6.26 \, m \, s^{-1}$ is assumed as the velocity of the relative airflow $v_{\infty}$. The heat-transfer coefficient $h$ for the forced flow convection by the propellers over the insulating shell depends on the Nusselt number, which itself is derived according to the Whitaker correlation[22] from the Reynolds and Prandtl numbers given in Equation (2) where $\rho$ corresponds to the air's density, $v_{\infty}$ to the speed of the relative airflow, $\delta$ to the characteristic length of the geometry, $\mu$ to the dynamic viscosity of air, $c_p$ to the specific heat of the air, and $k$ to the air's thermal conductivity. The Nusselt number for spheres $Nu_{shpere}$ is derived from Equation (3), applicable for values of $3.5 < Re < 80\,000$ and $0.7 < Pr < 380$, where $h$ corresponds to the heat-transfer coefficient, $\delta$ to the characteristic length of the geometry, and $k$ to the thermal conductivity of the air.

$$Re_{sphere} = \frac{\rho \cdot v_{\infty} \cdot \delta}{\mu}, \, Pr_{sphere} = \frac{\mu \cdot c_p}{k} \tag{2}$$

$$\begin{aligned} Nu_{sphere} &= \frac{h_{sphere} \cdot \delta}{k} \\ &= 2 + [0.4 \cdot Re^{1/2} + 0.06 \cdot Re^{2/3}] \cdot Pr^{0.4} \cdot \left(\frac{\mu_{\infty}}{\mu_s}\right)^{1/4} \end{aligned} \tag{3}$$

$$P_{j,total} = R_{internal} \cdot I^2 \cdot 4 \tag{4}$$

It is assumed that $\mu_{surface} \approx \mu_{\infty}$ due to the low heat conduction of the PI aerogel material. Therefore, the surface temperature is assumed to be equal to the air temperature of 200 °C and the values for the other variables are evaluated at this temperature. The characteristic length $\delta$ is assumed as the circumdiameter of the octagon hull cross section, hereby simplified as a sphere, resulting in a heat-transfer coefficient of $h_{sphere} \approx 25 \, W \, m^{-2} \, K^{-1}$. This value is utilized for the transient thermal simulations of the insulating shell from the surrounding environment. Finite-element analyses (FEAs) are utilized to further assess critical areas such as the camera windows, the arms of the quadrotor, as well as the gearboxes (Figure S3, Supporting Information). The insulating shell is designed as such that the temperature at the internal wall of the shell does not exceed the maximum battery operating temperature of 40 °C at an external temperature of 200 °C for the battery run time. Since the external temperature of 200 °C exceeds the maximum operating temperature of the internal components by far, excess heat cannot be radiated to the environment as usual with drones in room-temperature conditions. Therefore, the internal cooling system compensates for the heat generated by the motors through Joule heating as well as the heat dissipated by the electronic components by releasing $CO_2$ from a cartridge. Based on the mission profile and the expected joule heating $P_j$ of the four motors (Equation (4)), where $R_{internal}$ corresponds to the internal resistance of the motor and $I$ to the current, the $CO_2$ cartridge size can be selected with the latent heat of evaporation of $CO_2$ of $h_{e,CO_2} = 574 \, J \, kg^{-1}$.[23]

## 2.2. PI Aerogel

The beneficial properties of PI aerogels in terms of their insulating performance and resilience against high temperatures are utilized for the design of an insulating shell for the temperature-agnostic drone. The microstructure of PI aerogels can be varied by adjusting the type of diamine and dianhydride and their molar ratios, the degree of polymersization, the type and concentration of cross-linkers, and the imidization agent[24,25] and high-temperature shrinkage can be limited by the inclusion of silica aerogel (SA) particles.[26] In the current study, we used mixed diamines of oxydianiline (ODA) and dimethylbenzidine (DMBZ) in 1:1 molar ratio and polymerized them with biphenyl-3,3′,4,4′-tetracarboxylic dianhydride (BPDA). No cross-linker is used to ensure the sol viscosity is low enough to ensure good sol infiltration for the glass fiber composites. The synthesis process of the PI aerogel is illustrated in **Figure 3**. The detailed steps for the synthesis of the plain PI aerogel and the GFRPI aerogel composites for higher mechanical properties are highlighted in the experimental section. The sample acronyms and their physical and chemical properties are listed in **Table 1** and Figure S4, Supporting Information.

To assess the microstructure of the different aerogel samples, they are analyzed with a scanning electron microscope (SEM). SEM imaging of nonconducting aerogels requires a compromise: a conducting metallic or carbon coating is necessary to avoid charging effects, but a too thick layer of a coating may mask
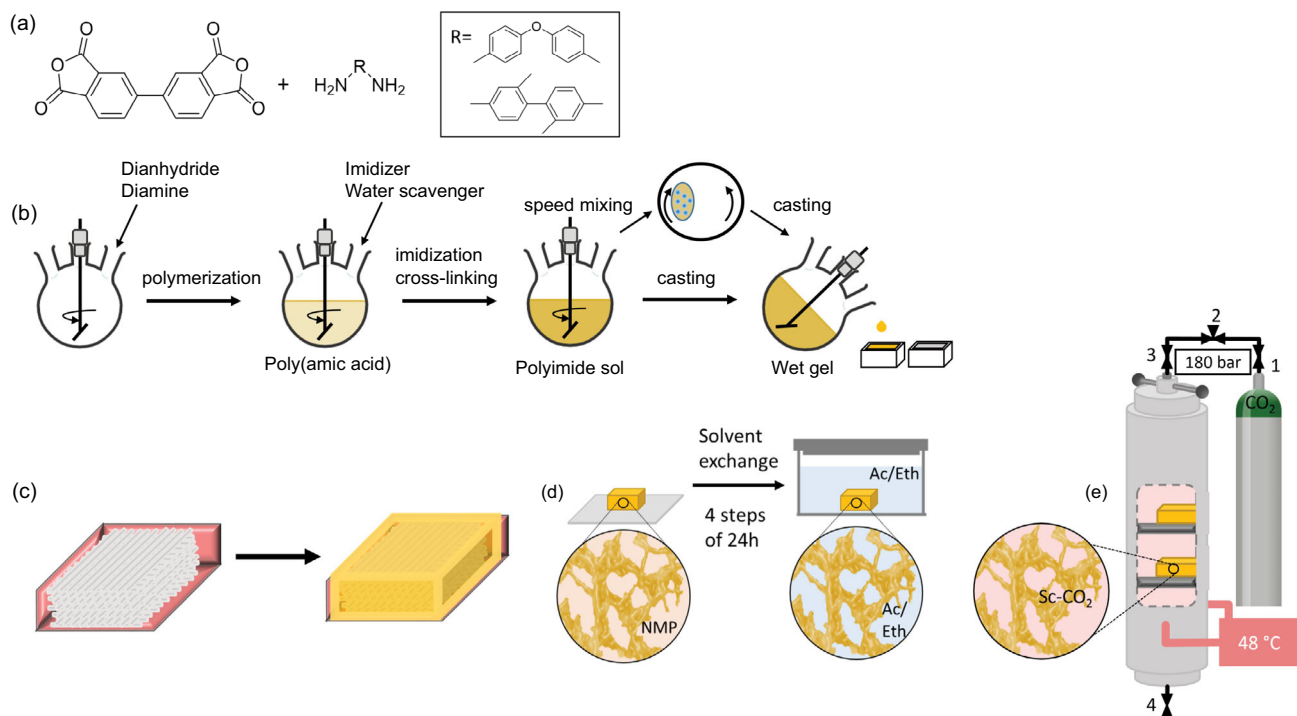
**Figure 3.** Synthesis of the PI aerogel components for drone manufacturing. a) Structure of the diamines and dianhydride used for PI preparation. b) Schematic steps required to do the synthesis of PI wet gels. c) Compounding PI–glass fiber composites by impregnation. d) Schematic of the solvent exchange performed. e) Illustration of the supercritical $CO_2$-drying conditions of the composite aerogels.

**Table 1.** Physical properties of the pure and composite polyimide aerogels, before and after treatment at 200 °C.

| Sample[a] | $\rho$ [g cm$^{-3}$] | $\lambda$ [mW m$^{-1}$ K$^{-1}$] | $S_{BET}$ [m$^2$ g$^{-1}$] | $V_{BJH}$ [cm$^3$ g$^{-1}$] | $D_{BJH}$ [nm] |
|---|---|---|---|---|---|
| PI | 0.07 ± 0.01 | 25.5 | 329 | 2.10 | 27.3 |
| PI-200 | 1.17 ± 0.12 | – | 1.2 | 0 | 3.9 |
| PI-SA | 0.10 ± 0.01 | 19.9 | 446 | 2.61 | 17.8 |
| PI-SA-200 | 0.39 ± 0.01 | 56.5 | 202 | 1.12 | 14.6 |
| GFRPI | 0.16 ± 0.02 | 22.9 | 113 | 0.41 | 16.1 |
| GFRPI-200 | 0.21 ± 0.09 | 36.4 | 1.0 | 0.01 | 20.8 |
| GFRPI-SA | 0.16 ± 0.03 | 23.8 | 168 | 0.60 | 12.4 |
| GFRPI-SA-200 | 0.23 ± 0.07 | 30.0 | 86 | 0.39 | 13.4 |

[a]PI stands for pure polyimide aerogel; PI–SA is the polyimide silica aerogel composite; GFRPI is the glass fiber–reinforced polyimide aerogel composite; GFRPI-SA is the glass fiber–reinforced polyimide silica aerogel composite; and PI-200, PI-SA-200, GFRPI-200, and GFRPI-SA-200 are the corresponding samples after treatment at 200 °C.

or alter the appearance of the nanoscale microstructure .[27] The PI aerogels display a nanofibrous 3D porous network with fiber diameter in a range of 20–50 nm (Figure S5, Supporting Information). Even though PI itself is stable when exposed to high temperatures (with a decomposition of >500 °C, **Figure 4**i), the aerogel microstructure is not stable and large volumetric shrinkage occurs at elevated temperatures. The chemical

cross-linking and monomer selection can, to some extent, reduce the shrinkage of the PI aerogels during synthesis, gelation, and drying,[17,28–30] but not at high-utilized temperature (Figure S4, Supporting Information). GFRPI aerogel displays good compatibility at room temperature (Figure 4a), and can efficiently reduce high-temperature shrinkage (200 °C), at least at the macroscopic level (Figure S6, Supporting Information). However, at the nanometer scale, GFRPI aerogel still displays a large degradation of the pore structure (Figure 4c). Between the tangled glass fibers, the polymer aerogel filler cannot be observed, and the fibrous pore structure (Figure 4b) is completely eliminated after exposure to 200 °C (Figure 4d). After incorporation with SA particles, the GFRPI-SA composite displays a fiber-reinforced composite morphology: the nanofibrous PI aerogel structure and the particulate SA are observed among the entangled glass fibers (Figure 4e), with the different aerogel phases visible at higher magnification of the same sample (Figure 4f). After heat treatment, most of the composite aerogel features are preserved (Figure 4g) and at higher magnification, the SA structure is almost preserved entirely, and some fibrous PI structures could still be identified (Figure 4h).

Pure PI aerogel shows low densities in a range of 0.06–0.10 g cm$^{-3}$, and the thermal conductivity is around 25 mW m$^{-1}$ K$^{-1}$ (Table 1, Figure 4j). The addition of SA increases the density of the composites, but decreases the thermal conductivity to below 20 mW m$^{-1}$ K$^{-1}$. A reinforcement of glass fiber increases both the density and thermal conductivity, but all the composites show relatively good insulation performance below 25 mW m$^{-1}$ K$^{-1}$. The correlation between density and
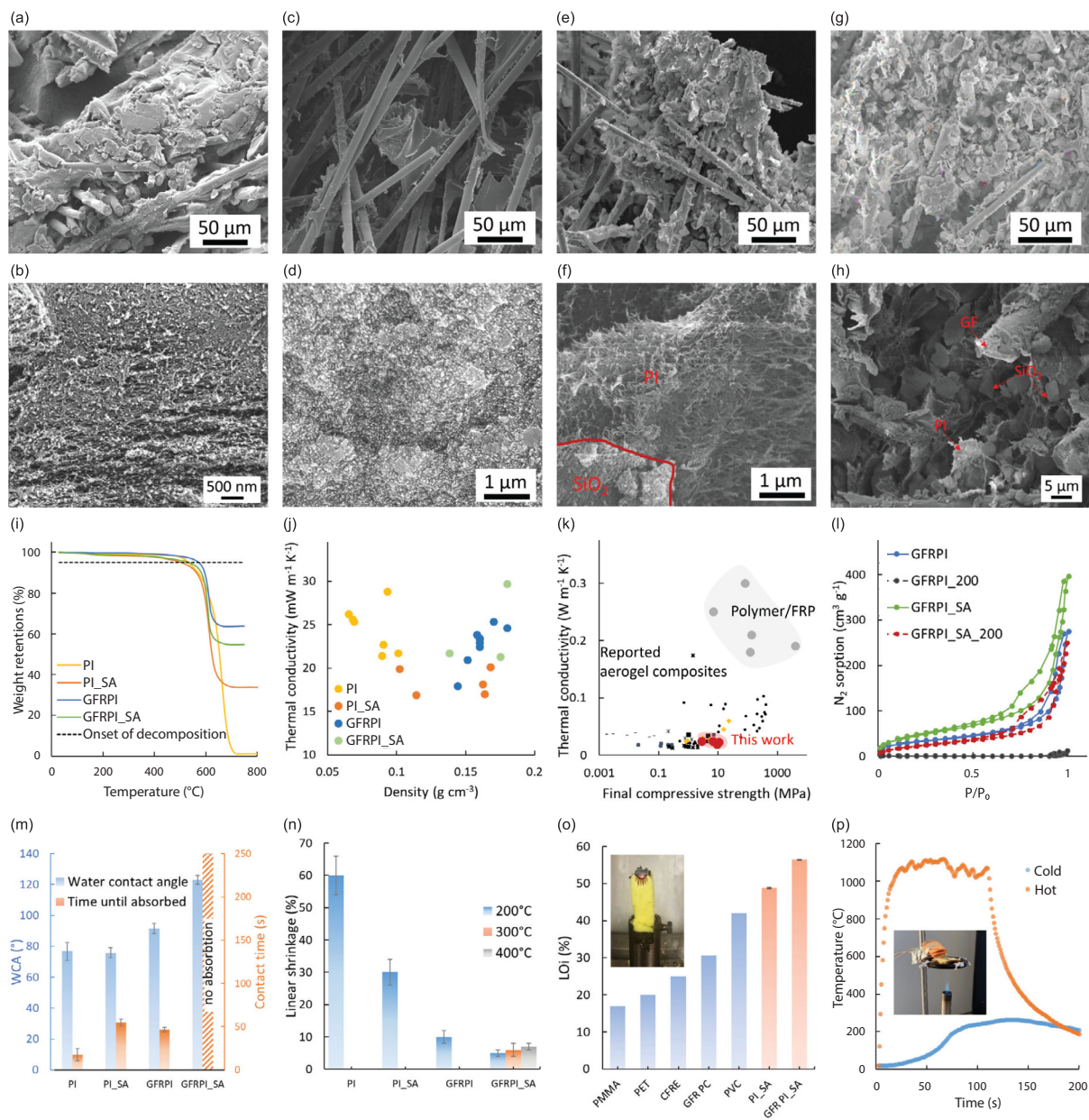
**Figure 4.** Physical properties of the PI aerogel composites. a,b) Scanning electron microscope (SEM) images of the glass fiber–reinforced polyimide (GFRPI) aerogel composite. c,d) SEM images of a GFRPI sample after 200 °C heat treatment. e) SEM image of a GFRPI silica aerogel (GFRPI-SA) sample. f) High magnification of GFRPI-SA sample with focus on aerogel phases. g,h) SEM images of a GFRPI-SA sample after 200 °C heat treatment. i) Thermogravimetric analysis (TGA) of the material systems. j) Plot of the thermal conductivity against the density. k) Plot of the thermal conductivity versus the final compressive strength.[41–45] l) Plot of the N$_2$ sorption isotherms. m) Water contact angle measurements. n) Plot of the linear shrinkage during heat treatment. o) Comparison of the limiting oxygen index among the reported polymer composites used for the drone and our composite PI aerogels. p) High temperature resistance of the component tile (GFRPI-SA with aluminum coating) exposed to 1000 °C.

thermal conductivity for the prepared materials follows a U dependence (Figure 4j), which is often reported for aerogel materials.[31] The PI composite aerogels display an excellent combination of mechanical and thermal properties, with for example high final compressive strength compared to most reported aerogel materials, and a superior thermal insulation property compared to typical polymers and fiber-reinforced polymer composites utilized in the drone development (Figure 4k, for a more

detailed view, see Figure S7, Supporting Information). All samples display type IV nitrogen sorption isotherms expected for mesoporous aerogel materials (Figure S8, Supporting Information, Figure 4l), the addition of glass fibers (and their mass) reduces the mass-normalized sorption volume by half. The Brunauer–Emmett–Teller (BET) surface area increases upon the addition of SA but is also reduced by half after the introduction of glass fiber reinforcement. The added SA particles display

a high surface area of 765 m$^2$ g$^{-1}$, but the glass fibers have almost no surface area (0–0.5 m$^2$ g$^{-1}$) (Figure S9, Supporting Information). Since the specific surface area is nominalized by mass, the samples loaded with glass fiber have a lower specific surface area. After the heat treatment, only the GFRPI-SA composite maintains significant surface areas 86 m$^2$ g$^{-1}$. PI aerogels are generally hydrophilic, the water contact angle (WCA) can reach up to 80° during a short period of measurement, but this is mostly due to the surface roughness, and the water droplet is absorbed in seconds leading to irreversible structural damage (Figure 4m). The separate addition of SA (2 wt% in the sol) and glass fibers both increases the WCA, but the samples still quickly absorb the water after the measurement (Figure S10, Supporting Information). GFRPI-SA samples display hydrophobic behavior with stable WCA larger than 120°, the water droplet is no longer absorbed. The thermal stability is first evaluated by thermogravimetric analysis (TGA) and the onset of decomposition is taken as the temperature at which the weight loss is 5% (Figure 4i). Pure PI aerogels have a decomposition onset of 533 °C, consistent with the reported values.[14,15] The addition of SA drops the onset to 505 °C, which may be related to the decomposition of trimethylsilyl group on the SA surface.[32] An improved onset temperature is observed after incorporation with glass fiber, 572 °C for GFRPI and 534 °C for GFRPI-SA. For practical purposes, the high-temperature dimensional stability is more important than the chemical decomposition temperature. Pure PI aerogel shows dramatic linear shrinkage (60%) after exposure to 200 °C, but the addition of SA reduces this by half (Figure 4n). GFRPI aerogel can retain its shape much better, with less than 10% shrinkage, but the SEM images (Figure 4c,d) and nitrogen sorption data (Figure 4l) indicate that while the shape is maintained by the glass fiber, the PI pore structure degrades completely. The GFRPI-SA sample displays less than 5% linear shrinkage, and this benefit could be maintained up to 400 °C. To show a direct advantage of using PI aerogel for the thermally agnostic aerial robot, it is important to understand the fire resistance behavior of the PI composites (Figure 4o). Both pure PI and glass fiber–reinforced GFRPI-SA show a very high limiting oxygen index (LOI), greater than 48, which is consistent with the reported high fire resistance of PI,[33] and even though the PI samples can still be carbonized by fire, the actual behavior is rather glowing than burning (Figure S11, Supporting Information). Compared to other polymers and fiber-reinforced polymers commonly used in drone applications,[34] PI-based materials show superior fire behavior. A high-temperature resistance test is carried out by exposing the drone component tile (10 mm GFRPI-SA coated with aluminum) sample directly to a 1000 °C flame, the temperature evolution is shown in Figure 4p. The top side of the sample could maintain a low temperature below 100 °C for 60 s, and with continuous heating for 120 s, the bottom reaches around 1100 °C, and the top side can slowly reach up to a plateau temperature of 230 °C. After removing the flame, due to the high insulation properties, the component needs another 100 s to be cooled down below 100 °C (Figure S12, Supporting Information). With this extremely hot but short temperature exposure, there is almost no obvious shrinkage in sample × and y directions, but a deformation on the surface and z-axis, resulting in around 12% volumetric shrinkage (Figure S13, Supporting Information),

considerably less than during the long time exposure to 200 °C (Figure S6, Supporting Information). Therefore, a short-time high-temperature exposure (as expected in firefighting applications) will only carbonize the surface while the dimension will only minimally change.

### 2.2.1. Drone Manufacturing

The super-critical CO$_2$ drying chamber limits the component size which requires the assembly of four small PI aerogel squares with a high-temperature-resistant silica-based adhesive (Thermocoll, Insulcon B.V., Netherlands) to form the larger tiles utilized for the protective shell (**Figure 5**a). Subsequently, the synthesized and bonded material is sanded to a height of 15 mm and milled to a side length of 75 mm with a recessed edge to allow the bonding of the mounting frames and angled sides for the final assembly of the protective shell (Figure 5b,c). The tiles are then coated with 1 μm of aluminum (Figure 5d) and the mounting frames additively manufactured from PA12 (PA12, Sintratec, Switzerland) are bonded to the tiles (Figure 5e). Once completed, the tiles are connected by the mounting tabs to form the top and bottom covers (Figure 5f). The aluminum top and bottom plates of the internal drone structure are cut on a water–jet machine, while the other metallic components are machined. Following the assembly of the structural elements such as the insulating exoskeleton (Figure 5g) and the internal structure, the drivetrain, avionics and DACS with the internal cooling system are integrated and the arms insulated with three layers of PI foam (3.5 mm thickness each) and reflective coating to complete the system (Figure 5h).

### 2.2.2. System Performance

Temperature measurements on structural elements of the drone are recorded in controlled environmental conditions in a heat chamber to validate the simulation results (**Figure 6**a). The thermocouples are attached to the aerogel shell structure which was thermally simulated in the design phase (Figure 6b).

The boundary conditions are set to 50 °C environment temperature to ensure no damage occurs to the insulation material before outdoor trials. The thermocouple readings for the outside of the insulating shell correlate to the simulation results (Figure 6e). Slight simulation deviations from the measurements are assumed to be caused due to modeling simplifications. For the internal shell temperature (Figure 6f), it is assumed that manufacturing imperfections with small gaps in the insulating shell led to a faster initial temperature rise compared to the simulation, whereas the slope of the data corresponds well. Nonetheless, the tests of the insulating shell show that the heat transfer from the environment is delayed and the internal systems are protected. More details on the FEA settings are described in detail in Figure S14, Supporting Information. An additional low temperature test at −12 °C is performed in a climate chamber to further assess the insulation performance (Figure S15, Supporting Information). As expected, an inverted trend is observed compared to Figure 6e,f. Based on observations from tests in controlled environments and outdoor testing near open fire at a firefighter training center (Figure 6c) and a glacier
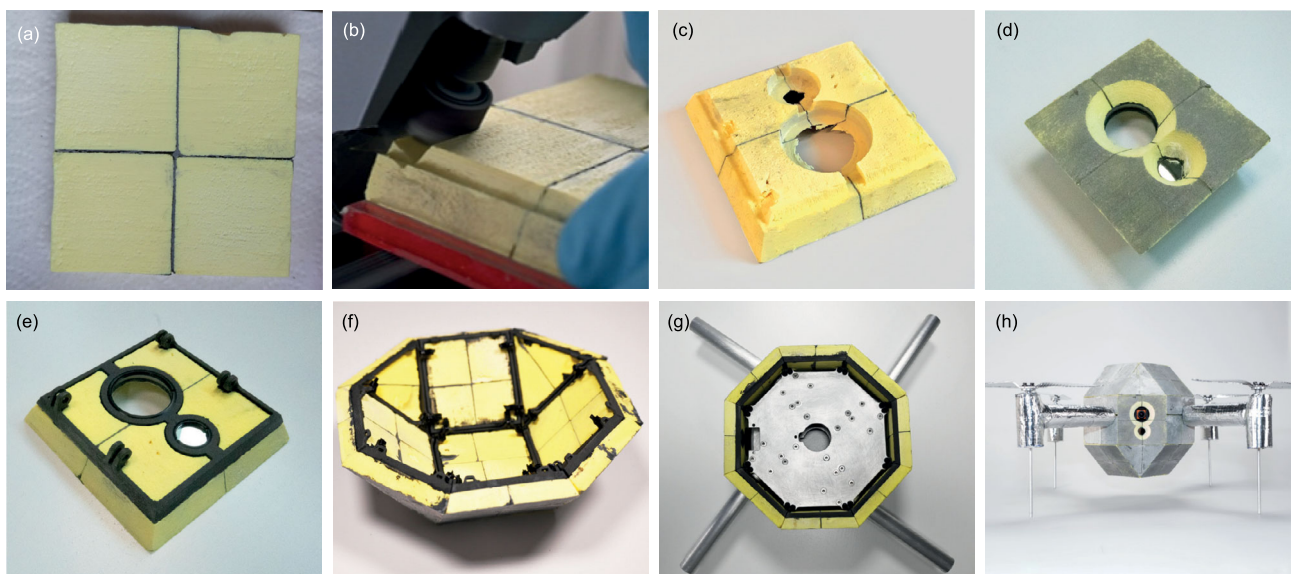
**Figure 5.** Manufacturing and assembly of the structural components. a) Bonding of the individual tiles. b) Milling of base material to the required specification. c) Internal view of the finished tile element. d) External view of the aluminum surface-coated tile element. e) Bonding of mounting frames to the tile element. f) Photograph of the assembly of the top cover. g) Mounting of the exoskeleton to the internal structure. h) Overview of the fully assembled drone.
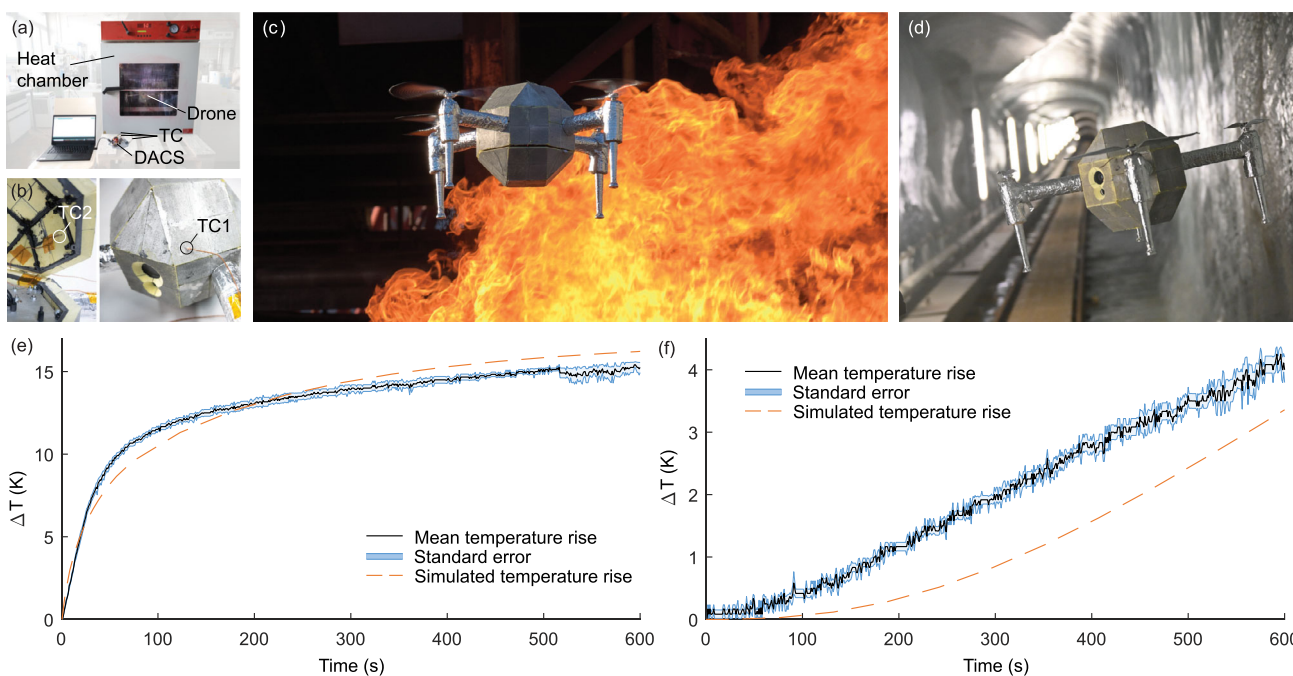


**Figure 6.** Characterization and testing of the assembled drone. a) Testing setup for the simulation validation. b) Thermocouple placement inside and outside of the insulating shell, directly opposite. c) FireDrone flight testing in a live fire scenario at a firefighter training center. A video of this test is attached in the supporting documents (Video S1, Supporting Information). d) FireDrone in a glacier tunnel, representative for cold environments. e) Plot of the measured external shell temperature in relation to the simulated temperature. f) Plot of the measured internal shell temperature in relation to the simulated temperature.

tunnel (Figure 6d), the performance of the thermally agnostic system to shield sensitive components from extreme environment conditions could be validated. More information on the outdoor tests is provided in Section S1 and Figure S16,

Supporting Information. In high-temperature environments, the time of operation is mainly determined by the performance of the insulation as well as the size of the $CO_2$ cartridge of the internal cooling system to keep all components within operating

**ADVANCED
SCIENCE NEWS**

www.advancedsciencenews.com

**ADVANCED
INTELLIGENT
SYSTEMS**

www.advintellsyst.com

temperature. In low-temperature environments, the heat generated by the motors and electronics may additionally be utilized to keep the batteries within operating range. With low outside temperatures, the need for a cooling system can be minimized and the time of operation would be limited by the battery capacity. For an optimal performance of the mechanical transmission, the bevel gears of the drivetrain require precise positioning. With the potential thermal expansion during operation in extreme temperature environments, the implementation of alternative 90° gear systems such as crown gears may be beneficial to compensate axial offsets.

## 3. Conclusion

In this article, we have presented a novel aerial robot utilizing high-performance PI aerogel insulation to operate in extreme temperature environments. It tackles the challenge of currently existing systems being limited by environmental factors such as high temperature, preventing flight, and data collection in hazardous hot-temperature environments. The deployment of drones capable of operating in such scenarios may be beneficial for emergency services during disasters, providing first responders with crucial information to assess the situation before entering the danger zone, thus minimizing risk to human lives. Design principles inspired by nature have been applied for insulation, internal cooling, and geometry to improve the system performance in extreme temperature environments. The performance of the FireDrone has been validated in temperature chamber tests and flights near active fire sources. Further development, miniaturization and the integration of additional sensors to the FireDrone may lead to the eventual deployment in real-life firefighting missions and help to save lives. Moreover, due to the excellent insulation properties of the PI aerogel, the operation of drones can also be expanded and elongated in extreme low-temperature environments such as polar regions and enable researchers to conduct operations in conditions that would be life threatening to humans.

## 4. Experimental Section

*Chemicals*: The precursors for PAA were sourced as follows: ODA (97%) and BPDA (98%) from Sigma–Aldrich, and DMBZ (98%) from TCI Chemicals. The imidization agents triethylamine (TEA, ≥99%) and pyridine (≥99%) and the water scavenger acetic anhydride (AA) (≥98%) were purchased from Sigma–Aldrich. N-methyl-2-pyrrolidone (NMP, 98%, Chemie Brunschwig AG) was used as a solvent for PI synthesis, and acetone (99%, Thommen Furler) was used as exchange solvent. All reagents were used without further purification.

*Synthesis*: The synthesis started from a 7 wt% amino-terminated PAA in NMP solution. The precursors BPDA, ODA, and DMBZ were mixed with a dianhydride to diamine molar ratio of $n:(n+1)$ in NMP, where the repeat unit $n$ was in a range of 10–30 and the molar ratio between two diamines ODA and DMBZ was 1:1. After 30 min of polymerization at room temperature (S.T.P.), a mixture of AA and pyridine was slowly added to the PAA solution whilst stirring. The mixture was transferred into silicon molds and the gelation occurred within 5–30 min, depending on the number of repeat units $n$ and the imidization process. Gels were aged in the gelation solvent for 24 h (S.T.P.) before the solvent was exchanged with 75/25, 25/75, and 0/100 NMP/acetone in 24 h intervals. The gels were finally dried by supercritical $CO_2$ drying (Autoclave 4334/A21-1, Separex, France). The manufacturing is illustrated in Figure 3. For the PI–SA composites (PI–SA) synthesis, 2 wt% SA particles (amorphous, 5–20 μm; ENOVA,

Cabot Aerogel GmbH) were added into the PI sol after the addition of AA and pyridine and the blend was mixed directly in a planetary speed mixer (DAC 150.1 FVZ; Flack-Tek Inc.) at 2350 rpm for 1 min. The other processing steps were identical to those described above for the neat PI aerogel. For the GFRPI, E glass fiber needle mats (LIH FENG JIING Enterprise Co., Ltd.) were cut into shape and placed into a silicone mold. The PI sol (for GFRPI) or the PI–SA sol (for GFRPI-SA) was poured over the mats. The blankets were compressed with a spatula 5 times to remove air trapped in the blankets and maximize infiltration of the sol. After gelation, the same procedures as for the neat PI aerogel described earlier were followed.

*Characterization*: The bulk density was calculated from the mass and volume of the rectangular and cylindrical samples. SEM images were recorded with an FEI Nova NanoSEM 230 (FEI, Hillsboro, Oregon, USA) at an accelerating voltage of 10 kV and a working distance of around 5 mm. Nitrogen sorption analysis was carried out on a TriFlex instrument (Micromeritics, US) after a prior degassing step of 15 h at 80 °C and 0.016 mbar. The specific surface area was obtained using BET and the pore volume and pore-size distribution using Barrett–Joyner–Halenda (BJH) analysis.[35] The thermal conductivity was measured at 25 °C and 50% relative humidity (RH) using a custom-built guarded hot plate device (guarded zone: $50 \times 50$ mm$^2$, measuring zone: $25 \times 25$ mm$^2$) designed for small specimens of low thermal conductivity materials.[36] Uniaxial compression tests of the composites are performed on a monolithic cylindrical sample using a universal materials testing machine (Zwick/Z010, Zwick/Roell, Germany), equipped with a 10 kN force transducer (KAP-S, AST Gruppe GmbH, Germany) in a controlled environment (23 °C, 50% RH). Elastic moduli were measured in compression mode and are calculated from the linear region of the stress–strain curves, which typically occurred at 3% ± 2% strain. A constant deformation rate of 1 mm min$^{-1}$ was used and compressive strength values were taken at the first noticeable sign of cracking or until reaching 80% strain. The surface wettability of samples was evaluated by WCA measurement using an optical contact angle system (Dataphysics TBU 90E, Germany), combined with a high-speed camera. Water droplets were deposited directly on the top or bottom surfaces of the samples. Three measurements were performed per sample and averaged. The volume of the water droplet was 5 μL, and the tip was a precision stainless steel tip (Gauge 32, EFD). Fourier-transform infrared (FTIR) spectra were recorded with an FTIR spectrometer (Bruker, Tensor 27 FTIR) by means of attenuated total reflectance using a diamond crystal. TGA was carried out on 4–6 mg aliquots using a Netzsch TGA 209 F1 instrument in reconstituted air (80% $v/v$ O$_2$% and 20% $v/v$ N$_2$) with a heating rate of 5 °C min$^{-1}$ from 30 to 750 °C. High-temperature shrinkage experiments were conducted by placing square samples in a kiln (Pyrotec Brennofenbau Osnabrück, Germany). The linear shrinkage (S) was calculated by $S = (L0 - LT)/L0$; L0 and LT were the averages of the dimension of a sample before and after heat treatment. Variable thicknesses of aluminum were coated on the PI composites with a BAK 501 UNI E-beam evaporation device (Evatec Liechtenstein AG), and IR reflectance spectra (Figure S2, Supporting Information) were measured on a Shimadzu, UV-3600 spectrometer equipped with a 50 W halogen lamp and a deuterium lamp. The LOI was measured according to ASTM D 2863 using an oxygen index device (FTT OI, Fire Testing Technology, UK). The samples ($60 \times 15 \times 15$ mm) were conditioned for at least 40 h at 23 ± 2 °C and 50% ± 5% RH before the measurements. The high-temperature resistance of the GFRPI-SA component was measured by a home-designed device (Figure S13, Supporting Information), and a K-type micro thermocouple was attached to the top surface as well as on the lower surface of the GFRPI-SA component. The temperature was recorded by a temperature datalogger (RS-172TK). The IR images of the GFRPI-SA component surface were also recorded using an IR thermal imager (Testo 880-1, Testo SE & Co., UAE).

## Supporting Information

Supporting Information is available from the Wiley Online Library or from the author.

## Acknowledgements

## Conflict of Interest

The authors declare no conflict of interest.

## Data Availability Statement

The data that support the findings of this study are available from the corresponding author upon reasonable request.

## Keywords

[1] P. Ward, How Animals Survive in Cold Conditions - Science of the Cold **2023**, https://www.coolantarcti≈com/Antarctica%20fact%20file/science/cold_all_animals.php (accessed: February 2023).

[2] M. Tonelli, G. Gomes, W. D. Silva, N. T. Magri, D. M. Vieira, C. L. Aguiar, J. M. S. Bento, *Sci. Rep.* **2018**, 8.

[3] P. Prestrud, *Arctic* **1991**, 44, 132.

[4] Z. Xuan, S. Ke, N. Bin, *Unmanned Aerial Vehicle Capable of Flying in Cold Weathers* **2017**, https://worldwide.espacenet.com/CN106956781A (accessed: April 2023).

[5] W. C. Myeong, K. Y. Jung, H. Myung, in *2017 14th Int. Conf. on Ubiquitous Robots and Ambient Intelligence*, URAI, Jeju, Korea (South) **2017**, pp. 204–207, https://doi.org/10.1109/URAI.2017.7992713.

[6] M. Hyeon *Flying Robot for Fire Resistance Based on Fire Resistance Fiber and Cushion Air Gap* **2016**, https://patents.google.com/patent/KR101821881B1/en (accessed: April 2023).

[7] A. Miriyev, M. Kovač, *Nat. Mach. Intell.* **2020**, 2, 658.

[8] M. Kovač, *Soft Rob.* **2014**, 1, 28.

[9] N. Hüsing, U. Schubert, *Aerogels - Airy Materials: Chemistry, Structure, and Properties*, Angewandte Chemie, Weinheim **1998**.

[10] M. M. Koebel, A. Rigacci, P. Achard, *Aerogels Handbook*, Springer, New York **2011**, pp. 607–633.

[11] Stepanian Christopher, Highly Flexible Aerogel Insulated Textile-Like Blankets **2005**, https://patents.google.com/patent/US20070154698A1/en [accessed: February 2023].

[12] L. Hines, V. Arabagi, M. Sitti, *IEEE Trans. Rob.* **2012**, 28, 987.

[13] L. Bai, Y. Zhang, S. Guo, H. Qu, Z. Yu, H. Yu, W. Chen, S. Tan, *Adv. Mater.* **2023**, 2211437.

[14] M. A. B. Meador, C. R. Alemán, K. Hanson, N. Ramirez, S. L. Vivod, N. Wilmoth, L. McCorkle, *ACS Appl. Mater. Interfaces* **2015**, 7, 1240.

[15] M. A. B. Meador, E. J. Malow, R. Silva, S. Wright, D. Quade, S. L. Vivod, H. Guo, J. Guo, M. Cakmak, *ACS Appl. Mater. Interfaces* **2012**, 4, 536.

[16] A. D. Sakaguchi, G. D. Poe, D. J. Irvin, A. M. Joaquin, J. D. Manning, Polymer Aerogel with Improved Mechanical and Thermal Properties **2016**, https://patents.google.com/patent/US20200277464A1/en [accessed: February 2023].

[17] H. Guo, M. A. B. Meador, L. McCorkle, D. J. Quade, J. Guo, B. Hamilton, M. Cakmak, G. Sprowl, *ACS Appl. Mater. Interfaces* **2011**, 3, 546.

[18] S. L. Vivod, M. A. B. Meador, C. Pugh, M. Wilkosz, K. Calomino, L. McCorkle, *ACS Appl. Mater. Interfaces* **2020**, 12, 8622.

[19] S. Wu, A. Du, Y. Xiang, M. Liu, T. Li, J. Shen, Z. Zhang, C. Li, B. Zhou, *RSC Adv.* **2016**, 6, 58268.

[20] Cactus-Tech.com Commercial and Industrial-Grade Products White Paper CTWP011, Technical Report https://www.cactus-tech.com/wp-content/uploads/2019/03/Commercial-and-Industrial-Grade-Products.pdf [accessed: February 2023].

[21] Propeller Thrust, https://www.grc.nasa.gov/www/k-12/airplane/propth.html [accessed: February 2023].

[22] S. Whitaker, *AIChE J.* **1972**, 18, 361.

[23] Liquids - Latent Heat of Evaporation **2003**, https://www.engineeringtoolbox.com/fluids-evaporation-latent-heat-d_147.html [accessed: February 2023].

[24] B. N. Nguyen, M. A. B. Meador, D. Scheiman, L. McCorkle, *ACS Appl. Mater. Interfaces* **2017**, 9, 27313.

[25] Z. Zhu, H. Yao, F. Wang, J. Dong, K. Wu, J. Cao, D. Long, *Macromol. Mater. Eng.* **2019**, 304, 1800676.

[26] Z. Kantor, T. Wu, Z. Zeng, S. Gaan, S. Lehner, M. Jovic, A. Bonnin, Z. Pan, Z. Mazrouei-Sebdani, D. Opris, M. Koebel, W. Malfait, S. Zhao, *Chem. Eng. J.* **2022**, 443, 136401.

[27] L. Juhász, K. Moldován, P. Gurikov, F. Liebner, I. Fábián, J. Kalmár, C. Cserháti, *Polymers* **2021**, 13, 588.

[28] H. Guo, M. A. B. Meador, L. McCorkle, D. J. Quade, J. Guo, B. Hamilton, M. Cakmak, *ACS Appl. Mater. Interfaces* **2012**, 4, 5422.

[29] S. Wu, A. Du, S. Huang, W. Sun, G. Zu, Y. Xiang, C. Li, B. Zhou, *RSC Adv.* **2016**, 6, 22868.

[30] X. Pei, W. Zhai, W. Zheng, *Langmuir* **2014**, 44, 13375.

[31] J. C. Wong, H. Kaymak, S. Brunner, M. M. Koebel, *Microporous Mesoporous Mater.* **2014**, 183, 23.

[32] S. Iswar, G. M. B. F. Snellings, S. Zhao, R. Erni, Y. K. Bahk, J. Wang, M. Lattuada, M. M. Koebel, W. J. Malfait, S. Iswar, G. M. B. F. Snellings, S. Zhao, R. Erni, Y. K. Bahk, J. Wang, M. Lattuada, M. M. Koebel, W. J. Malfait, *Acta Mater.* **2018**, 147, 322.

[33] X. Zhang, W. Li, P. Song, B. You, G. Sun, *Chem. Eng. J.* **2020**, 381, 122784.

[34] Y. Zhang, Y. Huang, Z. Li, L. Ke, K. Cao, Y. Guo, *Aerospace* **2021**, 8, 387.

[35] E. P. Barrett, L. G. Joyner, P. P. Halenda, *J. Am. Chem. Soc.* **1951**, 73, 373.

[36] T. Stahl, S. Brunner, M. Zimmermann, K. Ghazi Wakili, *Energy Build.* **2012**, 44, 114.

[37] D. Stanley, King Penguins **2014**, https://commons.wikimedia.org/wiki/File:King_Penguins_(15793396170).jpg [accessed: February 2023].

[38] H. Macky, Spittle Bug, Philaenus Spumarius **2016**, https://citscihub.nz/File:1-spittle_bug_Helen_Macky.jpg#filelinks [accessed: February 2023].

[39] J. Pie, Arctic Fox **2016**, https://commons.wikimedia.org/wiki/File:Arctic_Fox,_Iceland_2_(Unsplash).jpg [accessed: February 2023].

[40] P. Trimming, Young Fox **2011**, https://commons.wikimedia.org/wiki/File:Young_fox_(2)_(6173021652).jpg [accessed: April 2023].

[41] N. D. U. Berardi, *Polymers* **2015**, *7*, 2276.

[42] C. Zhang, A. Li, Y.-H. Zhao, S.-L. Bai, Y.-F. Zhang, *Composites, Part B* **2018**, *135*, 201.

[43] Y. Wang, B. Tang, Y. Gao, X. Wu, J. Chen, L. Shan, K. Sun, Y. Zhao, K. Yang, J. Yu, W. Li, *ACS Omega* **2021**, *6*, 19238.

[44] K. Bulanda, M. Oleksy, R. Oliwa, G. Budzik, Ł. Przeszłowski, J. Fal, T. Jesionowski, *Polymers* **2021**, *13*, 2455.

[45] Y. K. Sahu, Master Thesis **2014**.